Available online at www.sciencedirect.com

ScienceDirect

Nuclear and Particle Physics Proceedings 267–269 (2015) 332–341

www.elsevier.com/locate/nppp

Dark Energy, a Summary

G. Gutierrez

Fermi National Accelerator Laboratory, PO Box 500, Batavia, IL 60510, USA

Abstract

The accelerated expansion of the Universe, described by the term Dark Energy, is one of the most important open questions in Cosmology today. This mysterious Dark Energy comprises about 70 % of the Universe and all the available data to date favors the notion that it is a Cosmological Constant. We will review the current status of the experimental data on Dark Energy and provide a short description of the upcoming experiments poised to shed light on this problem.

Keywords: Dark Energy, Accelerated Expansion, Cosmological Constant

1. Introduction

The accelerated expansion of the Universe was discovered in the late 1990s by two groups measuring accurate distances to distant Type Ia supernovae [1, 2]. Even though the term Dark Energy is routinely used to describe this acceleration, the cause of this phenomenon is still unknown.

Contrary to regular matter, Dark Energy has negative pressure. Regular matter has positive pressure and when compressed the energy in a given volume increases, which in turn increases the gravitational attraction. If the mass is large enough this will give rise to the runaway process that causes gravitational collapse and gives birth to black holes. Positive pressure then will cause the Universe to decelerate, Dark Energy therefore has to have negative pressure. Equation 1 shows Einstein′s equations with a cosmological constant Λ, and the energy-momentum tensor T^{μ}_{ν} for a perfect isotropic fluid

$$G^{\mu}_{\nu} = 8\pi G\, T^{\mu}_{\nu} - g^{\mu}_{\nu}\Lambda;\; T^{\mu}_{\nu} = \begin{pmatrix} -\rho & 0 & 0 & 0 \\ 0 & p & 0 & 0 \\ 0 & 0 & p & 0 \\ 0 & 0 & 0 & p \end{pmatrix} \quad (1)$$

ρ and p are the energy density and pressure of the fluid. We see that for a cosmological constant the pressure is equal to minus the density, therefore $w = p/\rho = -1$. In general for the Universe to accelerate we need $w < -1/3$. To high precision, all the experimental data to date is consistent with w been constant and equal to -1. So in searching for deviations from a cosmological constant it is customary to expand w and keep only linear terms

$$w(t) = w_0 + [1 - a(t)]\, w_a = w_p + [a_p - a(t)]\, w_a \quad (2)$$

When using w_0 the expansion is around today′s value of $a(0) = 1$. Other values of the expansion point are often used (a_p in Eq. 2) which have the advantage of making the error ellipse in the plane (w_p, w_a) to be upright. Expressed in this way, the Dark Energy challenge is to determine if w_a is different from zero.

The acceleration of the Universe started at about $z \approx 0.8$, or half way the current age of the Universe. So to understand Dark Energy in detail we would like to understand how the Universe evolved from before it started to accelerate until now, which covers a range of redshift between $0 < z < 3$. The CMB data, at $z \approx 1000$, is essential to understand the evolution of the Universe during the acceleration epoch because it fixes many important parameters. For a review of the CMB status see other articles in these proceedings.

Cosmology has entered an era of precision measurements. The current error in w_0 is about 5% and fu-

http://dx.doi.org/10.1016/j.nuclphysbps.2015.10.127

ture experiments will bring this value to the sub percent level. The literature on the subject is vast so we will summarize here only recent results obtained with well established techniques and give a brief review of some of the upcoming experiments relevant for Dark Energy. Of course in selecting which topics to cover, familiarity with the experiments and results has played a role.

2. Probes of Dark Energy

The probes for Dark Energy can be divided into two main groups, geometry measurements and large scale structure formation. The geometry measurements essentially map the geometry of the Universe as a function of time and they currently provide the best constraints on Dark Energy. The growth of large scale structure depends on the dynamics of the evolution of the Universe and together with the geometry measurements allow for tests of General Relativity on large scales.

The main probes of geometry measurements come from the use of Type Ia Supernovae (SNe Ia), Baryon Acoustic Oscillations (BAO) and the direct determination of H_0. The main probes for the growth of cosmic structure are Redshift Space Distortions (RSD), Weak Gravitational Lensing and abundance of Galaxy Clusters. Due to lack of space in this review we will only cover SNe Ia, BAO and RSD which together with the CMB provide today the best constraints on DE.

2.1. Geometry probes

For a flat, homogeneous and isotropic Universe the metric is given by

$$ds^2 = -dt^2 + a^2(t)\,(dx^2 + dy^2 + dz^2) \qquad (3)$$

so the measurement of the geometry of the Universe is essentially encapsulated in the measurement of the scale factor $a(t)$ as a function of time. Figure 1 displays the scale factor as a function of time. The plot also shows the current measurements and gives predictions for the DESI experiment (see Section 3.2). We can see that $a(t)$ has been well measured up to about 10 billions years ago and that in the next decade it will be measured up to about 12 billion years ago. The inset also shows that to go below 1% in the measurement of w, the scale of the Universe will have to be measured with unprecedented precision.

To measure distances on large scales two techniques are used, one uses standard candles (SNe Ia), and the other one uses a standard ruler (BAO). As we will see in the following section the initial luminosity of supernovae Type Ia can be predicted very accurately from

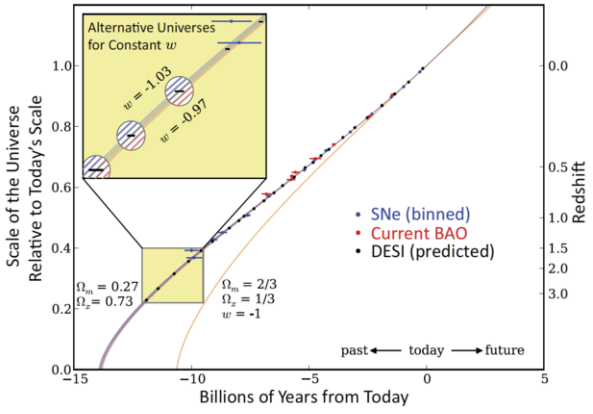

Figure 1: Expansion history of the Universe, or $a(t)$, normalize to one today, as a function of the Universes look-back time in billions of years. Supernovae measurements are shown in blue, current BAO measurements are shown in red and projections for DESI are shown in black. (Reprinted from Ref. [3]).

measurements of their decay time. Knowing the initial luminosity of these standard candles, measuring their redshifts and assuming sound cosmological models allows for a precise determination of their distances (a precise determination of H_0 is also needed to establish the absolute scale of these distances).

The sound waves generated in the photon-baryon plasma up to the recombination epoch generated a characteristic scale (the standard ruler) that can be very precisely measured by the CMB experiments [6]. This standard ruler was imprinted in the dark matter which in turn imprinted it in the visible matter in the Universe up to today. So, tracking this standard ruler through the history of the Universe allows for a precise determination of $a(t)$.

2.1.1. Type Ia Supernovae (SNe Ia)

Type Ia supernovae are white dwarf stars in binary systems that accrete mass from their companion star and eventually explode into supernovae. The luminosity decay time for these supernovae is related to its absolute luminosity, a fact that makes it possible to use these supernovae as standard candles. The top plot in Fig. 2 shows the absolute magnitude of Type Ia supernovae as a function of time. We see that brighter supernovae have a longer decay time than fainter ones. The bottom plot in the same figure shows that a simple stretching of the time and a related scale of the magnitude bring all the supernovae into a standard curve. Therefore armed with the standard curve and the stretch in decay time one can determine the absolute luminosity of Type Ia supernovae.

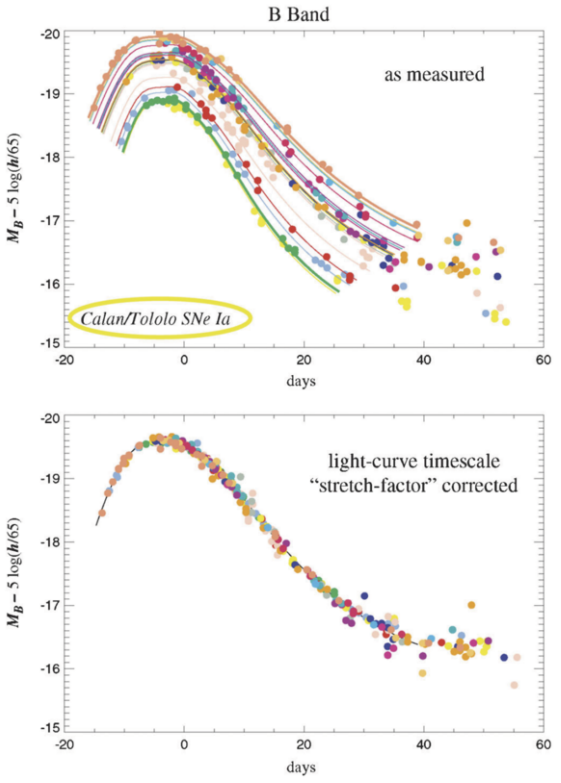

Figure 2: The top plot, displaying the absolute magnitude for Type I-a supernova as a function of time, shows that bright supernova take longer to decay than faint ones. The lower plot shows that a stretching of the time and a corresponding scale in the magnitud bring all Type I-a supernovae to a standard curve (Reprinted from Ref. [4]).

These supernovae are so bright that they can be seen half way across the Universe. Figure 3 shows the Hubble diagram with supernova SN SCP-0401 added to it. At a redshift of z=1.71 this is one of the furthest supernova known today, it exploded about 10 billion years ago.

Cosmological parameters can be extracted from the relation of the distance inferred from the luminosity and the measured redshift. The distance modulus is defined as $\mu = 5\log_{10}(d_c) - 5$ where d_c is the co-moving distance given by

$$d_c = \frac{c}{H_0}\int_0^z \frac{dz}{\sqrt{\Omega_m(1+z)^3 + \Omega_\Lambda f(z)}} \quad (4)$$

we have assumed a flat Universe ($\Omega_k = 0$) and neglected the radiation term ($\Omega_r \approx 0$) because it is small at low z. Also

$$f(z) = \exp\left(3\int_0^z dz\frac{1+w(z)}{1+z}\right) \quad (5)$$

$$= (1+z)^{3(1+w_0+w_a)}e^{-3w_a z/(1+z)} \quad (6)$$

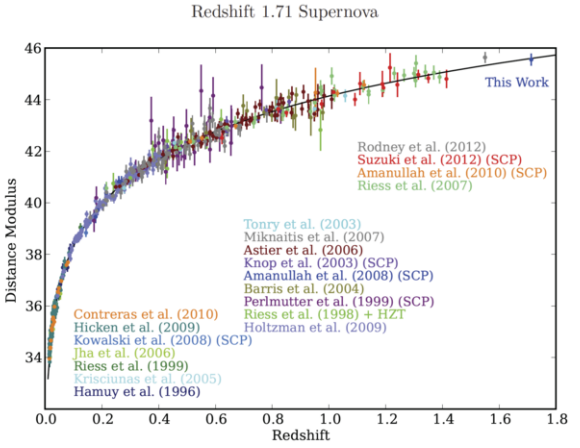

Figure 3: Hubble diagram with supernovae SN SCP-0401 added to it (labeled "This Work"). The black line is the best-fit using a flat ΛCDM model. (Reprinted from Ref. [5]).

In the last line we used $w(z) = w_0 + w_a(1-a) = w_0 + w_a z/(1+z)$. Fixing H_0 and assuming a ΛCDM model ($w_0 = -1$, $w_a = 0$) leaves only Ω_m as a free parameter. The best calibrated set of SNe Ia comes from the Joint Light-curve Analysis collaboration (JLA) [7]. This collaboration performed a combined analysis of the Sloan Digital Sky Survey (SDSS) and the Supernovae Legacy Survey (SNLS) data. Improvements in photometry, light curve uncertainty and the inclusion of the full SDSS SN Ia data allowed JLA to obtain a sample of 740 SNe Ia with reduced systematic errors. This sample together with supernovae from the Hubble Space Telescope (HST) and the Low-z collaboration is shown in Figure 4. The black curve is a one parameter fit to all the data. Assuming $H_0 = 70$ km s^{-1} Mpc^{-1} the fit gives a value of $\Omega_m = 0.295 \pm 0.034$. This value is compatible with the recent measurement by Plack of $\Omega_m = 0.308 \pm 0.012$ [6].

The supernovae sample doesn't have a redshift lever arm large enough to allow for fits with more than one parameter. To allow parameters like w_0, w_a, Ω_m and Ω_k to vary simultaneously, other data sets have to be added. The JLA collaboration included CMB and BAO data and performed two, one parameter extension fits (Ω_m,Ω_k) and (Ω_m,w), and a two parameter extension fit (Ω_m,w_0,w_a). The result of the one parameter extension fit (Ω_m,w) is shown in Figure 5 and gives a value of $w = -1.018 \pm 0.057$. The two parameter extension fit (Ω_m,w_0,w_a) gives $w_0 = -0.957 \pm 0.124$ and $w_a = -0.336 \pm 0.552$. For details of all the fit parameters see Tables 14 and 15 in Ref. [7].

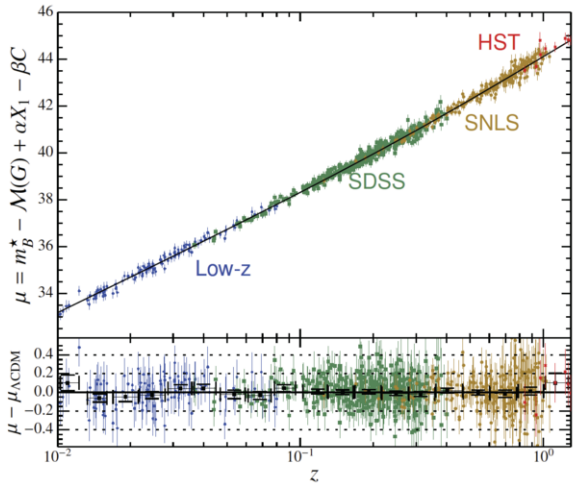

Figure 4: The top plot shows the distance modulus as a function of redshift for different supernovae Type Ia samples. The black line is the best fit to a ΛCDM cosmology with $H_0 = 70$ km s^{-1} Mpc^{-1}. The bottom plot shows the residuals of the best fit as a function of redshift. (Reprinted from Ref. [7]).

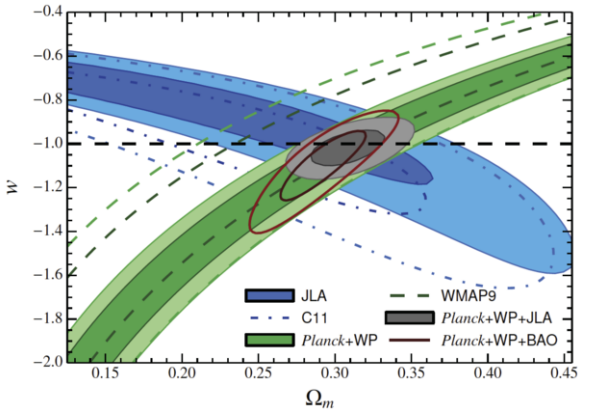

Figure 5: Confidence contours at 68% and 95% (including systematic uncertainty) for the Ω_m and w cosmological parameters for the flat wCDM model. The black dashed line corresponds to the cosmological constant hypothesis (Reprinted from Ref. [7]).

2.1.2. *Baryon Acoustic Oscilations (BAO)*

Minutes after the Big Bang the Universe consisted of a fluid made of dark matter, photons, neutrinos, electrons, protons, ^{4}He and traces amounts of ^{3}He, deuterium and lithium nuclei. Except for the very small density fluctuations produced by quantum fluctuations amplified during inflation, this fluid was extremely uniform. The density fluctuations propagated through the fluid in the form of sound waves. The velocity of sound c_s was close to the speed of light ($c_s \approx 1/\sqrt{3}$). This finite sound velocity plus the expanding Universe created a sound horizon beyond which two regions of the fluid could not communicate with each other. The sound horizon then acted as the "cavity of a musical instrument" generating peaks and valleys in the wave spectral distribution. These oscillations were imprinted in the distribution of both matter and radiation and were frozen at the time of recombination. With a characteristic scale of ≈ 150 Mpc, these oscillations are well within the linear regime of General Relativity, which makes this signal fairly insensitive to non-linear effect or other systematic errors. These Baryon Acoustic Oscillations can be studied using the two point correlation function between galaxies.

The two point correlation function is calculated using the difference in angles $\delta\theta$ and redshifts δz between two galaxies. The transverse and radial distances are calculated as $\delta x = \delta\theta\ d_c$ and $\delta r = \delta z\ c/H$, where H and d_c are the Hubble rate and the co-moving distance respectively. Figure 12 shows a simulation of the two dimensional correlation function $\xi(s,\mu)$, s being the distance between galaxies and μ the cosine of the angle between the galaxy pair and the line-of-sight. We can clearly see the BAO ring at about 110 Mpc h^{-1} in the $\xi(s,\mu)$ simulation. $\xi(s,\mu)$ is not uniform due to the effect that the galaxy peculiar velocities have on the redshifts. Galaxies attracted toward the overdensity at the center will appear closer and the ones attracted towards the ring overdensity will appear further away.

In the BAO analysis we want to measure the position of the ring. This can be done using a two dimensional analysis of $\xi(s,\mu)$, or if the statistics is not large enough using only the monopole $\xi(s)$ of the two dimensional distribution. Both analyses have been performed using the SDSS data [8], here we only review the one dimensional analysis. Figure 6 shows $\xi(s)$ and the power spectrum $P(k)$ (the Fourier transform of the spacial density) for the Sloan DR11 data. The BAO peak and the oscillations in the power spectrum are clearly visible. "Reconstruction" refers to the process of removing the effects of non-linear structure formation and peculiar velocities. Given that the scale of the BAO peak is accurately known from the CMB measurements one can change the cosmological parameters and determine d_c and H from a fit to the peak. These two quantities are then combined into the one dimensional expression $D_V(z) = (d_c^2 cz/H)^{1/3}$. This quantity for two different redshift bins is displayed in Fig. 7. One can see the remarkable agreement between these measurements and the predictions from the CMB using a flat ΛCDM model. Figure 8 shows the measurements normalized to the Planck predictions. We can clearly see that the

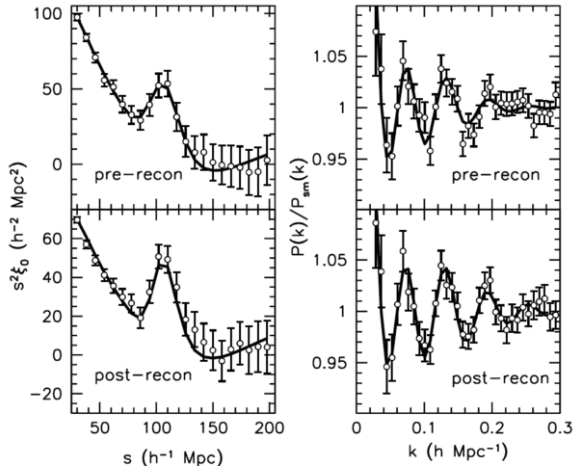

Figure 6: Clustering measurements (black circles) with $\xi(s)$ shown in the left panels and $P(k)$ in the right panels. The top panels show the measurements prior to reconstruction and the bottom panels show the measurements after reconstruction. The solid lines show the best-fit BAO model in each case. One can see that reconstruction has sharpened the acoustic feature considerably for both $\xi(s)$ and $P(k)$. (Reprinted from Ref. [8]).

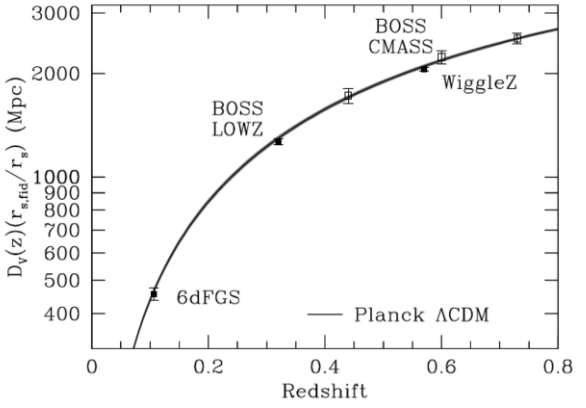

Figure 7: $D_V(z)(r_{s,fid}/r_d)$ versus z from the BOSS CMASS and LOWZ surveys together with the acoustic peak detection from the 6dFGS and WiggleZ. The grey region shows the 1 σ prediction from the Planck 2013 results assuming a flat ΛCDM model. One can see the superb agreement in these cosmological measurements. (Reprinted from Ref. [8]).

measurements are consistent with the CMB predictions from both Planck and WMAP+SPT/ACT.

2.1.3. Lyman-α forest

Quasi-Stellar Objects, QSOs or quasars, also referred to as AGN or Active Galactic Nuclei, emit light with an essentially white spectrum. These are some of the brightest objects in the sky and can be seen all the way across the Universe. The light from far away QSOs gets absorbed by hydrogen clouds in the path between the QSO and us. Figure 9 shows the light spectrum for a nearby QSO and a far away one. One can clearly see the hydrogen absorption lines in the far away QSO. These absorption lines correspond to the Lyman-α series of hydrogen and are therefore called the Lyman-α forest. If we have hundreds of thousands of QSOs then the Lyman-α forest provides a 3D map of the hydrogen clouds in the Universe and the baryon acoustic oscillation peak should be observable in the two point correlation of these hydrogen clouds.

In this section we summarize the results of BOSS DR11 quasar studies [9]. This data set consists of 137,562 quasars in the redshift range of $2.1 < z < 3.5$. These quasars provide approximately $2.4\text{x}10^7$ Lyman-α absorption lines, which is more that the one million galaxies used for the BAO measurement of the previous section.

The transmitted flux fraction $\delta(\lambda)$ is calculated for every quasar $\delta(\lambda) = f(\lambda)/[C(\lambda)\bar{F}(z)] - 1$, where $f(\lambda)$ is the observed flux and $C(\lambda)\bar{F}(z)$ are normalization constants. The two point correlation function is then calculated as $\xi = (\sum w_{ij}\delta_i\delta_j)/\sum w_{ij}$, where w_{ij} are weights and δ_i is the transmitted flux fraction for wavelength bin i.

Figure 10 shows the measured two point correlation function in the angular range $0.8 < \cos\theta < 1$, with $\cos\theta = r_p/\sqrt{r_p^2 + r_t^2}$ and (r_p, r_t) being the parallel and transverse distance to the line-of-sight. The BAO peak is clearly visible in this $\cos\theta$ range, as well as in two other ranges shown in Ref. [9].

A beautiful advantage of QSOs is that being so bright they allow for measurements of the geometry of the Universe well before the Universe started to accelerate. Figure 11 shows the expansion rate of the Universe as a function of redshift. The solid red point in the figure shows the result summarized in this section. It is clear that detail measurements of the Lyman-α forest in QSOs will allow to map the expansion of the Universe before the Dark Energy era. The DESI experiment described in Section 3.2 will map this region with exquisite detail [3].

2.2. Growth of Large Scale Structure

Within a few minutes after the big bang and the recombination epoch ($z \approx 1000$) the interaction between the photons and the electrons provided a restoring force that made it possible for sound waves to propagate in the medium. After recombination, that restoring force disappeared and only the pull of gravity was left. With the restoring force gone the shape of the matter struc-

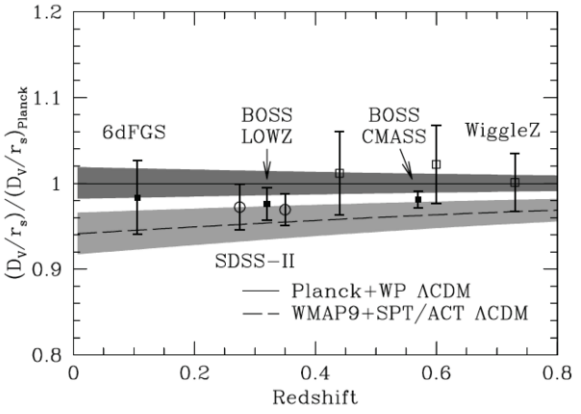

Figure 8: The $D_V(z)/r_d$ measured from galaxy surveys, divided by the best-fitting flat ΛCDM prediction from the Planck data. The horizontal line is by construction the Planck prediction, the dashed line shows the best-fitting flat ΛCDM prediction from the WMAP+SPT/ACT results. One can see a mild tension between the two CMB results. The current galaxy BAO data from BOSS fall in between the two predictions and is clearly consistent with both. (Reprinted from Ref. [8]).

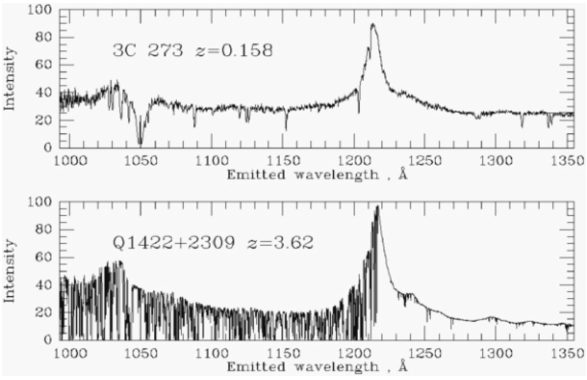

Figure 9: The top (bottom) plot shows the spectrum for a near by (far away) quasar at redshift of z=0.158 (3.62). The hydrogen absorption lines are clearly visible in the high redshift quasar.

ture froze in place and it just grew with time. Therefore one can write

$$\delta(x,a) = G(a)\,\delta(x) \tag{7}$$

where the density contrasts δ is defined as $\rho(x,a) = \rho_0(a)[1+\delta(x,a)]$ and the growth factor $G(a)$ can be written as

$$G(a) = \exp\left\{-\int_a^1 \frac{da'}{a'} f(a')\right\} \tag{8}$$

the growth rate $f(a)$ is given by

$$f(a) = \frac{a}{G}\frac{dG}{da} \approx [\Omega_m(a)]^\gamma \tag{9}$$

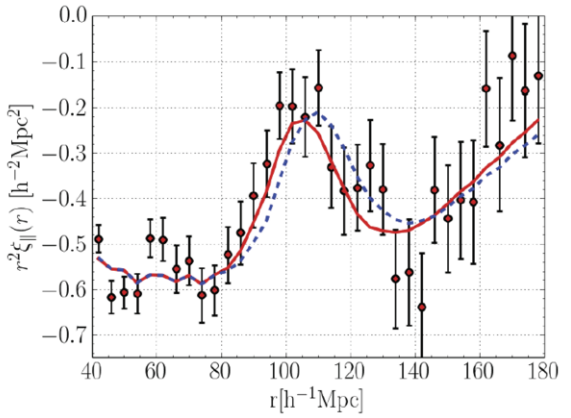

Figure 10: Measured correlation functions for the Lyman-α forest in the angular region $\cos\theta > 0.8$, where θ is the angle between a pair of points in the forest of two different QSOs and the line-of-sight. The BAO peak is clearly visible. (Reprinted from Ref. [9]).

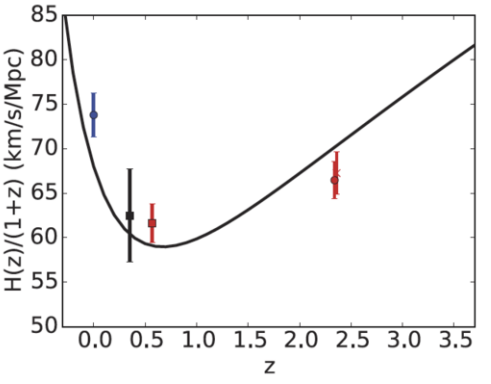

Figure 11: Expansion rate of the Universe (da/dt) as a function of redshift. The red square corresponds to the result of Section 2.1.2, the red circle to the Lyman-α result of this section. The other points are described in Ref. [3]. (Reprinted from Ref. [3]).

with $\Omega_m(a) = \Omega_m H_0^2/(a^3H^2)$ and $\gamma \approx 0.55$ for General Relativity. Therefore deviations from the growth rate given in Equation 9 or in the values of γ from 0.55 will constitute a deviation from General Relativity at large scales. As we will see in the following section the growth rate can be measured in Redshift Space Distorsions.

2.2.1. *Redshift Space Distorsions*

Figure 12 shows a simulation of the two dimensional correlation function $\xi(s,\mu)$, where s is the distance between galaxies and μ is the cosine of the angle between the galaxy pair and the line-of-sight. The transverse and radial distances between galaxies are calculated as $\sigma = \delta\theta\, d_c$ and $\pi = \delta z\, c/H$, where H and d_c are the Hub-

ble rate and the co-moving distance and $\delta\theta$ and δz are the difference in angles and redshifts between galaxies. This plot is not uniform because the galaxies peculiar velocities due to gravitational attraction by large scale structure modifies the redshifts due to the Hubble flow. So this plot contains information about the growth of large scale structure. The two point correlation function $\xi(s,\mu)$ is related to the power spectrum in redshift space $P_s(k)$. In linear theory we have [11]

$$P_s(k) = (b + f\mu)^2 P_m(k) \tag{10}$$

where b is the galaxy bias, f is the growth rate given by Eq. 9 and $P_m(k)$ is the matter power spectrum. So in RSD we measure $f\sigma_8$, where σ_8 is the normalization of the power spectrum.

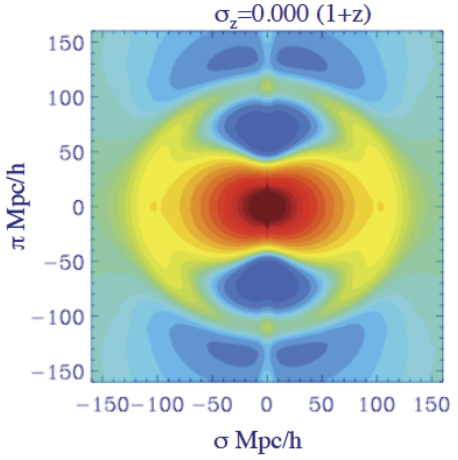

Figure 12: Simulation of the two point correlation function in two dimensions. The vertical axis shows the radial distance (π), the horizontal axis shows the transverse distance (σ). (See Ref. [10]).

The two point correlation function $\xi(s,\mu)$ can be expanded in Legendre polynomials:

$$\xi(r,\cos\theta,f) = \sum_{l=0,2,4} \xi(r,f) P_l(\cos\theta) \tag{11}$$

The top plot in Figure 13 shows the $\xi(s,\mu)$ distribution for the SDSS DR11 data [12]. We can clearly see the similarities with the simulations shown in Fig. 12. The bottom plot shows the monopole ($l = 0$) and the quadrupole ($l = 2$) for the same data. In BAO only the position of the peak at $\approx$110 h^{-1} Mpc is measured. In RSD the shape of the distribution is relevant, the detail prediction of this shape constitutes the largest systematic error in RSD today.

The value of $f\sigma_8$ for this analysis is shown by the gold pentagon in Figure 14 together with other measurements described in Ref. [3]. We can see that the error bars are currently too large to constrain different models of modified gravity, but as we will see in Section 3 this will change dramatically with the next round of DE experiments.

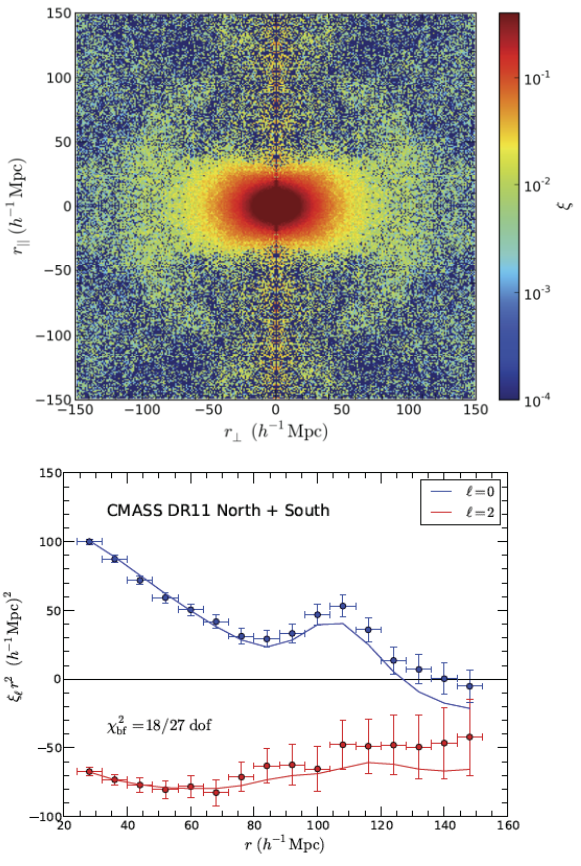

Figure 13: *Top*: The two-dimensional correlation function of the SDSS DR11 sample measured in bins of (h^{-1} Mpc)^2. *Bottom*: The measured monopole and quadrupole of the SDSS DR11 sample as a function of redshift-space separation r. The solid lines show predictions of the best-fitting model with $\Omega_b h^2 = 0.0222$, $\Omega_m h^2 = 0.1408$, $n_s = 0.962$, $b\sigma_8 = 1.29$, $f\sigma_8 = 0.437$, $\alpha_\perp = 1.017$, $\alpha_\parallel = 1.001$ and $\sigma^2_{FOG} = 12.6$. (Reprinted from Ref. [12]).

3. Future Experiments

All the precision data available today, from the CMB to measurements using galaxies or hydrogen clouds as we discussed in this summary, is consistent with us living in a flat Universe dominated by cold dark matter and a cosmological constant. This picture will be further

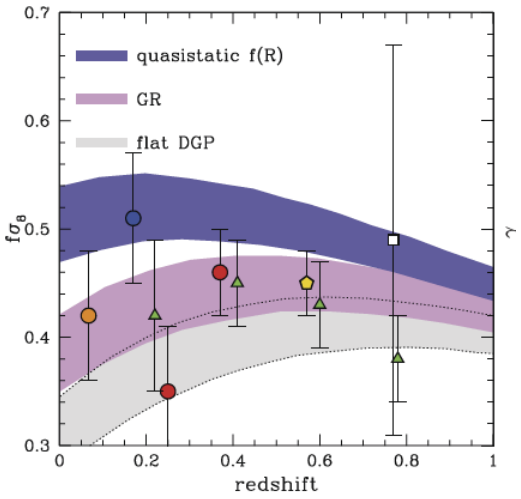

Figure 14: The data points show the SDSS DR11 measurement of $f\sigma_8$ (gold pentagon) along with similar, low redshift, measurements and 1σ error bars as presented in Table 2.1 of Ref. [3]. (Reprinted from Ref. [3]).

tested in the next 15 years by a series of experiments either running or being planned today. We have selected to summarize only a few of them. These experiments combined will push our knowledge of Dark Energy by at least an order of magnitude and will provide tight tests of General Relativity on large scales. Experiments like the Hobby-Eberly Telescope Dark Energy Experiment (HETDEX) and the Wide-Field Infrared Survey Telescope (WFIRST), which will also contribute to our understanding of DE, have not been included in the summary due to lack of space.

3.1. The Dark Energy Survey (DES)

The Dark Energy Camera (DECam) is a 570 Megapixel CCD camera upgrade to the 4 meter Blanco Telescope in Cerro Tololo, Chile. It is used by the DES collaboration to survey 5000 square degrees of the southern sky. DES is now in its second year of running and will complete the survey in the year 2018. DECam has a field of view of 2.2 degrees and collects data in five filters, labeled grizY. When the survey is completed the DES collaboration will have high resolution images of 300 million galaxies up to magnitud 24.5, 100,000 clusters of galaxies and about 4000 SNe Ia.

The DES collaboration plans to do Dark Energy studies using four different probes: 1) Baryon Accoustic Oscillation, 2) structure formation using galaxy clusters, 3) weak gravitational lensing and 4) measuring distances with supernovae Type Ia. Figure 15 shows the Dark Energy figure of merit expected by DES. The four ellipses show the 68% confidence levels for the DES expectations in the (w_0, w_a) plane for the four different probes. The solid red ellipse is the combined result of the four probes.

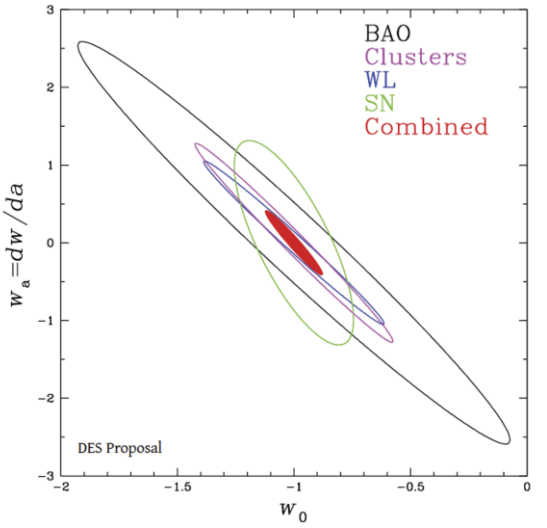

Figure 15: 68% CL predictions in the (w_0, w_a) plane for the DES experiment. The prediction for four different DE probes are shown: BAO in black, galaxy clusters in magenta, Weak Lensing in blue and SNe Ia in green. Each of these predictions include Planck priors. The red ellipse shows the predictions after combining all four probes. (Reprinted from Ref. [13]).

The expected errors after the combination are $\sigma(w_0) = 0.061$ for w_0 and $\sigma(w_a) = 0.217$ for w_a. Using a pivot point a_p in Eq. 2, corresponding to $z_p = 0.37$, the predicted error in w_p is $\sigma(w_p) = 0.018$. The prediction for the DETF [14] figure of merit is $[\sigma(w_a)\sigma(w_p)]^{-1} = 263.7$ (see Table 1 in Ref. [13]).

3.2. The Dark Energy Spectroscopy Instrument (DESI)

DESI is a Dark Energy experiment that will study Baryon Acoustic Oscillations and Redshift Space Distortions. The DESI instrument will be installed at the Mayall 4m telescope at the Kitt Peak National Observatory. This instruments consists of 5000 robotically-actuated fibers, ten three-arm spectrographs with a resolution $R = \lambda/\Delta\lambda$=2000-5500 (depending on the wavelength) covering a wavelength range from 360 nm to 980 nm. The DESI experiment will start running in 2019 and plans to cover 14,000 square degrees in five years, collecting spectra of Luminous Red Galaxies (LRGs) up to $z = 1$, Emission Line Galaxies (ELGs) up to $z = 1.7$ and QSOs in the range $2.1 < z < 3.5$. In total more than 20 million galaxies and QSOs will be collected up to magnitudes ≈22.5.

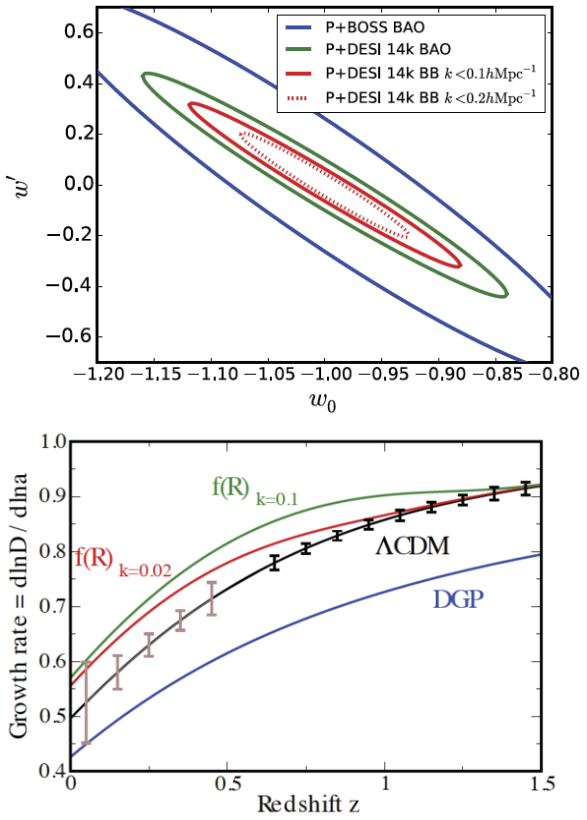

Figure 16: The top plot shows the 68% confidence limits on the (w_0, w_a) plane for BOSS BAO (in blue) and predictions for the DESI experiments using just BAO and BAO plus the Broad Band spectrum with two different limits on the value of k. Planck priors are included in all cases. The bottom plot shows the growth rate f as a function of redshift. DESI projections are shown with black error bars for the regular run and brown ones for the bright galaxy survey. The black line is the ΛCDM prediction, the color lines show predictions for two different alternative gravity models. (Reprinted from Ref. [3]).

The top plot in Figure 16 shows the 68% CL level predictions for the DESI experiment in the (w_0, w_a) plane. DESI expects an error in w_p of $\sigma(w_p) = 0.011$ with a DETF figure of merit of $[\sigma(w_a)\sigma(w_p)]^{-1} = 687$ [3], which is almost a factor of 3 improvement over DES. The bottom plot in Figure 16 shows the DESI predictions for the growth rate as a function of redshift (black and brown error bars) and the predictions for two models of modified gravity. DESI can clearly distinguish between General Relativity and these two models.

3.3. EUCLID

EUCLID is a satellite mission of the European Space Agency to be lunched in 2020. EUCLID comprises a 1.2 meter telescope with two main instruments: a Visible Imager (VIS) and a Near Infrared instrument (NIR) which provides three band photometry and slitless spectrography with $R = \lambda/\Delta\lambda \approx 250$. EUCLID will cover 15,000 square degrees of the sky in six years. It will measure the shape of 1.5 billion galaxies up to magnitude 24.5 in the visible and 24 in the infrared, and obtain low resolution spectra of 50 million galaxies in the range $0.7 < z < 2.1$. EUCLID will study dark energy primarily with Weak Lensing, Baryon Acoustic Oscillations and Red Shift Space Distortions.

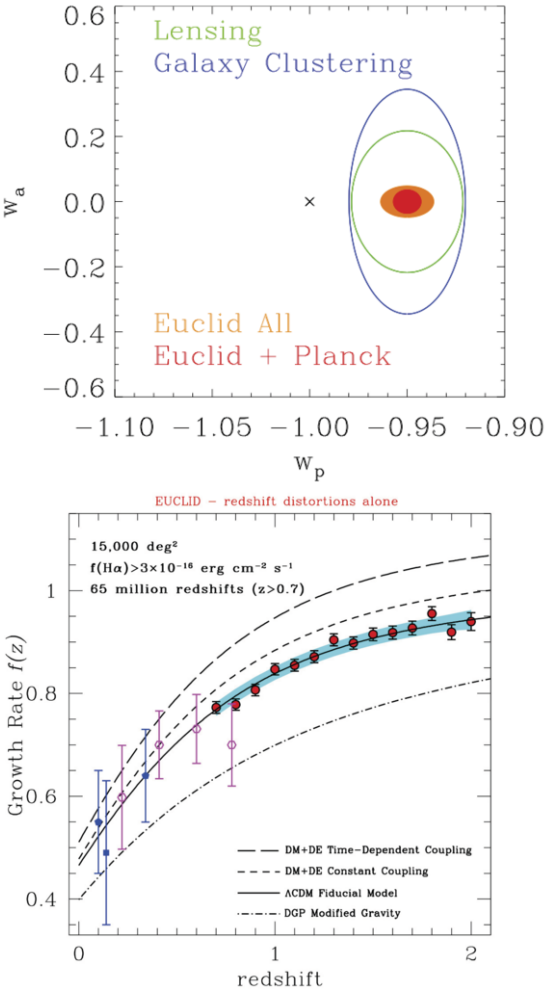

Figure 17: *Top:* Expected (w_p, w_a) constraints from Euclid. Weak lensing is shown in green, galaxy clustering in blue, all Euclid probes in orange and all Euclid with Planck in red. *Bottom:* Euclid predictions of the growth rate f(z) from RSD. The cyan area is the expected 1 σ error band, the red points correspond to EUCLID simulations. Also shown are measurements by the SDSS (filled pentagons), 2dF (filled square) and Wigglez (open hexagons). The lines show predictions for three different modified gravity models. (Reprinted from Ref. [15]).

The top plot in Figure 17 shows EUCLID DE predictions in the (w_p, w_a) plane. EUCLID expects an error in

w_p of $\sigma(w_p) = 0.013$, in w_a of $\sigma(w_a) = 0.048$ with a DETF figure of merit (FoM) of $[\sigma(w_a)\sigma(w_p)]^{-1} = 1540$. Combining EUCLID results with Planck will give $\sigma(w_p) = 0.007$, $\sigma(w_a) = 0.035$ and FoM=4020 [15]. The bottom plot in Figure 17 shows EUCLID predictions for the growth rate as a function of redshift and the predictions for three different models of modified gravity.

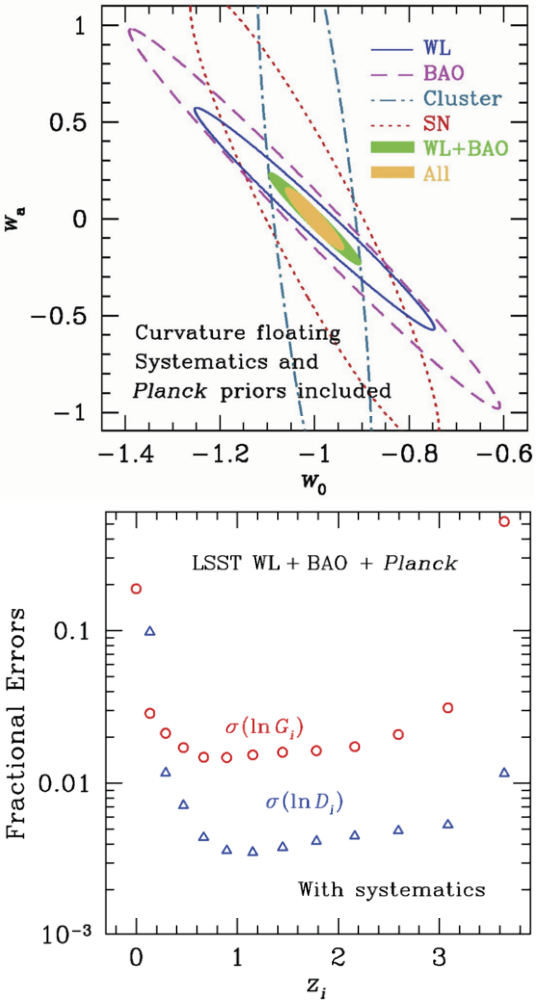

Figure 18: Top: Expected (w_0, w_a) constraints from LSST, showing the predicted errors for WL, BAO, galaxy clusters, SNe Ia, the combination of WL and BAO and all results combined. *Bottom:* 1σ relative errors as a function of redshift for the growth factor G (open circles) and the co-moving distance D (open triangles). (Reprinted from Ref. [16]).

3.4. The Large Synoptic Survey Telescope (LSST)

LSST is an 8 meter telescope that will provide a 3D map of the Universe with unprecedented detail. The telescope is been built at Cerro Pachon in northern Chile and it is currently scheduled to start operations in 2023. LSST will provide a comprehensive survey of the solar system, with detail studies of the structure and content of the Milky Way and studies in the evolution of galaxies and the nature of dark Energy and Dark Matter. LSST will cover 20,000 square degrees of the sky in 10 years, measuring 20 billion galaxies up to magnitude 27.5 with photometry in six band filters (ugrizY). Four probes of Dark Energy will be used by LSST: 1) Weak Lensing, 2) Baryon acoustic oscillations, 3) evolution of galaxy clusters and 4) Type Ia supernovae.

The top plot in Figure 18 shows the 68% confidence contours in the plane (w_0, w_a) for the LSST predictions for Weak Lensing (solid blue line), Baryon Acoustic Oscillations (dashed magenta line), galaxy clusters (dash-dotted green line), supernovae Type Ia (dotted red line). It also shows the WL and BAO combination (green shaded area) and the combination of all probes (gold shaded area). All these results include Planck priors. From the plot we can see that $\sigma(w_p) \approx 0.02$ ($w_a = 0$), and $\sigma(w_a) \approx 0.16$. The bottom plot in the same figure shows the predicted 68% relative errors for the growth factor G and the co-moving distance D.

4. Acknowledgements

I would like to thank the organizers for their invitation to participate in a wonderful Conference, for their fantastic hospitality and their infinite patience with the preparation of this manuscript. This work was funded in part by the US Department of Energy.

References

[1] Riess, A. G., Filippenko, et al., AJ, 116 (1998) 1009.
[2] Perlmutter, S., Aldering, G., et al., ApJ, 517 (1999) 565.
[3] DESI Conceptual Design Report, http://desi.lbl.gov/cdr/.
[4] Saul Perlmutter, Rev. of Mod. Phys., 84 (2012) 1127.
[5] D. Rubin et al., ApJ 763:35 (2013).
[6] Planck 2015 results. XIII. Cosmological parameters, arXiv:1502.01589v2.
[7] M. Betoule, et al, A&A 568 (2014) A22.
[8] L. Anderson et al., MNRAS 441 (2014) 24.
[9] T. Delubac et al, A&A 574 (2015) A59.
[10] E. Gaztañaga et al., MNRAS 399 (2009) 1663.
[11] N. Kaiser, MNRAS 227 (1987) 1.
[12] L. Samushia et al., MNRAS 439 (2014) 3504.
[13] See the "Dark Energy Survey Science Program" report in http://www.darkenergysurvey.org/reports/.
[14] A. Albrecht et al, arXiv:astro-ph/0609591.
[15] See "EUCLID Definition Study Report (Red Book)" in http://arxiv.org/abs/1110.3193.
[16] See "LSST Science Book" in http://www.lsst.org/lsst/scibook